Sensor-Embedded Tissue Phantom for Magnetic Resonance Elastography Mechanical Failure Testing

Charles P. Hong[1]
Department of Biomedical Engineering,
Georgia Institute of Technology,
Atlanta, GA 30332
e-mail: chong71@gatech.edu

Tarun Vinodkumar
School of Mechanical Engineering,
Georgia Institute of Technology,
Atlanta, GA 30332
e-mail: tvinodkumar3@gatech.edu

Heriberto Andres Nieves-Vazquez
Department of Biomedical Engineering,
Georgia Institute of Technology,
Atlanta, GA 30332
e-mail: hnieves6@gatech.edu

Jun Ueda
School of Mechanical Engineering,
Georgia Institute of Technology,
Atlanta, GA 30332
e-mail: jun.ueda@me.gatech.edu

Magnetic Resonance Elastography (MRE) is an imaging technique capable of quantifying the stiffness of in vivo tissue by applying and imaging shear waves produced by an MRE actuator. Poor image acquisition may result from the MRE procedure if there is insufficient contact between the MRE actuator and the patient. An experimental test setup outside of the clinic will aid in reducing the number of failed acquisitions by enabling the development of advanced actuators and actuator systems. This work presents the development and testing of a sensor-embedded tissue phantom setup paired with a support vector machine (SVM) classifier to automate the MRE actuator testing process. MRE actuation of soft tissue is simulated by utilizing a voice coil positioning stage that interfaces with a phantom. To capture the resulting vibrations, accelerometers are embedded inside the phantom. Subsequent characterization experiments verify the functionality of the developed phantoms to capture wave propagation. A secondary investigation was performed by utilizing the developed setup to collect acceleration measurements at varying contact distances. We provide an overview of feature analysis and selection to develop SVM models for contact detection. Multiple SVM models are reported, and the best-performing model displayed almost perfect validation (94.53%) and test (90.91%) accuracy. The pairing of sensor-embedded phantom with an SVM for detection demonstrates potential improvements to the MRE actuator developmental process by automatically assessing contact-related issues prior to clinical testing. [DOI: 10.1115/1.4066226]

Keywords: support vector machine, magnetic resonance imaging, testbed, contact classification, accelerometer, actuator

1 Introduction

Palpation is a diagnostic technique used to determine mechanical tissue stiffness changes based on the physician's tactile perception. While palpation can detect malignant tumors, the method is limited to superficial organs and only qualitatively measures tissue stiffness [1]. Magnetic resonance elastography (MRE) is a noninvasive magnetic resonance imaging (MRI)-based technique capable of quantifying internal soft tissue inspired by palpation [2]. Overcoming limitations of superficial tissue examination, MRE can assess deep-seated organs while acquiring quantitative mechanical stiffness information [3].

The MRE process is conducted in three separate steps: (1) harmonic mechanical shear waves are induced on the surface of the patient using a vibration transducer, (2) a modified MRI pulse sequence images the induced shear waves and records the data using toggled bipolar gradients, (3) an elastogram, or stiffness map, is then calculated through an inversion method applied to the recorded data [2,4,5]. MRE has several potential issues, from high costs to mechanical failures. This paper aims to address the mechanical failures of MRE by providing a new and more accessible method of testing MRE actuators and their configurations. Proper illumination, or diagnostic quality, of acquired MRE images allows physicians to diagnose patients accurately [6]. However, many unique constraints are introduced to the process by the necessary inclusion of an MRI machine. MRE image acquisition relies on an MRI-compatible actuator. These actuators generate vibrations into the patient over the region of interest (ROI) to illuminate the internal organs during imaging [7].

During the acquisition procedure of MRE wave images, there are multiple causes for which actuators can fail to transfer shear waves into the ROI, leading to poor quality images [8,9]. These failures arise from improper contact between the actuator and the surface, or skin, of the patient. Poor surface contact positions initiate early wave attenuation or deviations from the correct wave path in the tissue, leading to poorly illuminated images, low-quality stiffness maps, and failed examinations [10–12]. Currently, failure of MRE is determined by visual inspection by the technologist or interpreting radiologist. If a failure occurs and the professional is unable to draw usable information from the image, additional scans are necessary [13]. Furthermore, differences in anatomical features may cause unpredictable results in the scans leading to poor image acquisition. Additional repositioning of the actuator is typically required to overcome these differences and obtain interpretable images [14].

Therefore, precautions are taken in clinical settings to avoid mechanical failures. MRE clinical procedures describe the use of an elastic band to secure the MRE actuator to the patient [13,15,16]. However, the elastic band does not provide an inclusive and consistent solution as anatomical factors and the anatomical region to be imaged impact the capabilities to use the elastic band [17,18]. Anatomical factors may also require an altered MRE actuator position, leading to potential sources of improper contact depending on the type and size of the MRE actuator used [14]. Ultimately, while medical professionals attempt to mitigate mechanical failures, patient anatomy results in variability in MRE actuator contact.

To optimize MRE for different anatomical regions, varying MRE actuators and configurations are designed and tested. However, the current standard of MRE actuator testing is expensive and time-intensive as the entire MRE procedure is conducted on phantom tissues within the clinic [19]. The resulting wave images of the testing must be interpreted afterward, leading to an overall complex and high entry barrier to the research and development process of MRE actuators. As a result, a more accessible method to test MRE actuators is required to improve upon MRE at a higher pace. A laboratory testing method that automatically assesses proper wave propagation and contact will aid researchers in ultimately reducing actuator-based failure cases in clinical procedures.

To address this need, this work details the development and evaluation of sensor-embedded phantoms paired with a support vector machine (SVM) to automatically detect mechanical failure caused by poor MRE actuator contact at the surface of the skin. The phantom is actuated at the farthest face from the sensor, simulating actuator-skin contact, while the sensor that is placed farther down the phantom serves as the ROI. The waveforms produced by the MRE actuator are transmitted through the phantom and captured by the embedded sensors, removing the need for an MRI to record wave images. After the data collection, an SVM automates the process of interpreting the wave information. As a result, the first part of this work presents the phantom development and waveform validation experiments with subsequent analysis, and the second part presents the implementation of the SVM for the detection of suitable contact classification. Feature extraction and selection based on experimental data as well as multiple SVM models trained on the selected features will be presented, and accuracy metrics will be reported for each model.

2 Methods

The basis of this work is the sensor-embedded phantom, a silicone gel-block embedded with accelerometers to study actuated waveforms throughout the medium. A series of phantoms and an experimental testbed were developed to investigate the capabilities of the embedded sensors to measure wave propagation.

2.1 Embedded Phantom Fabrication.
The assessment of induced vibrations was critical to the task of detecting proper MRE actuator contact. Tri-axial InvenSense MPU6050 accelerometers (HiLetgo, China) with a gyroscope were used to collect the shear wave measurements induced into the phantom. This sensor was chosen for its low profile (21.2 mm × 16.4 mm × 3.3 mm) and high precision data output (16-bit). The chip communicates via I2C to an Arduino microcontroller and has two different addresses allowing for paired simultaneous readings from two sensors. The sampling rate of dual accelerometer readings was 141 Hz with only one axis being recorded from each accelerometer along with a timestamp of the data collection.

Many MRE studies utilize phantoms as they can emulate the material properties of a wide variety of internal tissue [20,21]. MRE phantom studies typically use agar phantoms because they are inexpensive to fabricate and have mechanical property tunability by varying the concentration of agar, mixing procedure, and curing parameters [22]. However, agar phantoms typically have a short shelf life and are fabricated with conductive materials [23]. For this study, we sought a phantom material with a long shelf life for prolonged usage and nonconductive properties so it would not affect the embedded sensors. SORTA-Clear 37 (Smooth-On Inc, Macungie, PA), a two-part silicone of 37 A durometer fulfilled the criteria. While the hardness of our selected material is above that of typical soft tissue (16-21 A durometer) [24], the selected visco-elastic material was chosen because MRE primarily targets areas of increased stiffness in soft tissue, such as for staging liver fibrosis [25]. For future studies, the hardness and viscoelastic parameters of the phantom can be tuned to be representative of desired ROIs and applications as the phantom can be easily fabricated from any type of silicone or nonconductive material.

The first step to developing the phantoms was to design and fabricate custom molds with polylactic acid (PLA) additive manufacturing. The walls of the molds were designed to be 1 mm in thickness for ease of extraction. The SORTA-Clear 37 two-part silicone solution was mixed thoroughly for five minutes and then poured into the molds. The necessary sensors were placed into the mixture and the entire phantom was left to cure for 24 h at room temperature (25 °C). After the phantom had solidified, the phantom was removed from the mold and excess silicone was trimmed off. To readily gather data from the accelerometer, the pins were left exposed as shown in Fig. 1.

While the majority of phantoms had the accelerometers embedded during the curing process, some phantoms required the sensors to be embedded after curing to achieve specific accelerometer positions within the phantom. To embed the sensor within the phantom after the curing process, an incision was made on the side of the phantom near the chosen location and a part of the cured silicone was removed. The sensor is then placed into the phantom through the incision.

2.2 Testbed Setup.
To test various custom phantom designs and ensure re-usability of the system, the testbed was designed to be modular. The testbed system was three-dimensional (3D) printed and has three main parts: the base, phantom holders, and actuator system. The base had alternating trenches of 5 mm width and 6 mm depth running down the length. The phantom holders and the actuator system had inserts to connect with the trenches. Custom phantom holders were designed, and 3D printed for each different cured phantom and fulfilled a set of criteria which are outlined as follows: (1) the holder only constrains the corners of the phantom and (2) the front of the holder is exposed for the actuator. The actuator system had four support columns and a platform that held the actuator. The support columns facilitated an interference fit with the platform and allowed for the platform's, and consequently, the actuator's, vertical position to be continuously modular and fit the varying needs of the experiments. The actuator was constrained in the actuator base with an interference fit. The entire testbed setup was constrained to the experiment's bench top with a vice to minimize residual vibrations. A labeled version of the testbed is shown in Fig. 2.

2.2.1 Actuator.
The testbed actuator must be configurable to test the phantom's capabilities at various positions and frequencies.
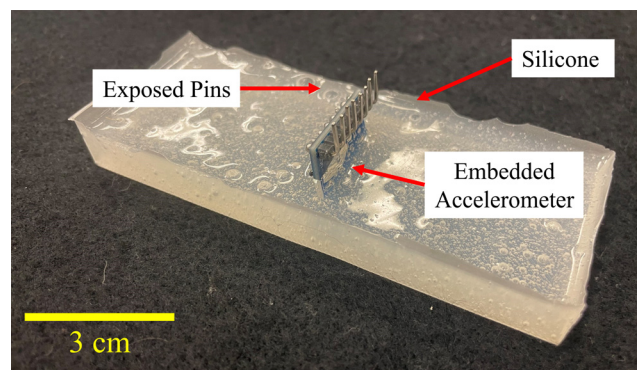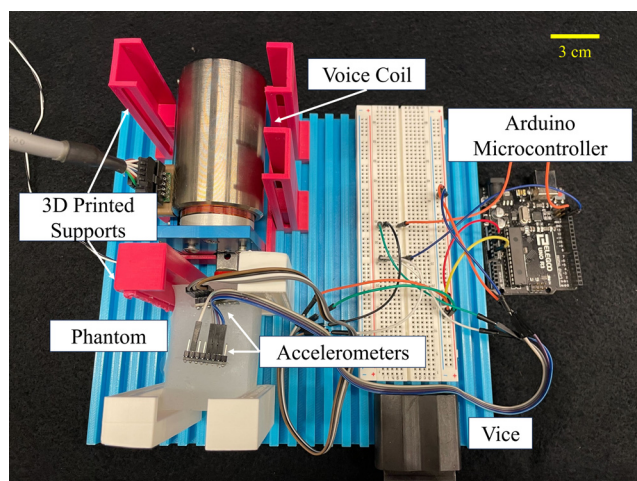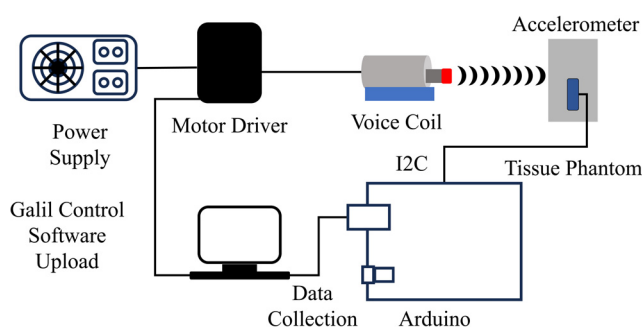

Fig. 1 Overview of an embedded phantom

Fig. 2 A phantom with embedded accelerometers positioned against the voice coil for actuation. 3D printed parts hold the phantom and actuation system while a vice grounds the system to reduce vibrations.

Fig. 3 Diagram of the experimental setup

A VCS24-029-LB-12 voice coil motor (H2W Technologies, Santa Clarita, CA) was used as the actuator with the P/N DMC-30011 Galil controller (Galil, Rocklin, CA) providing the necessary control and parameter tunability. The Galil controller was connected to an outside PC via ethernet and was interfaced through the Galil Design Kit software to program the positio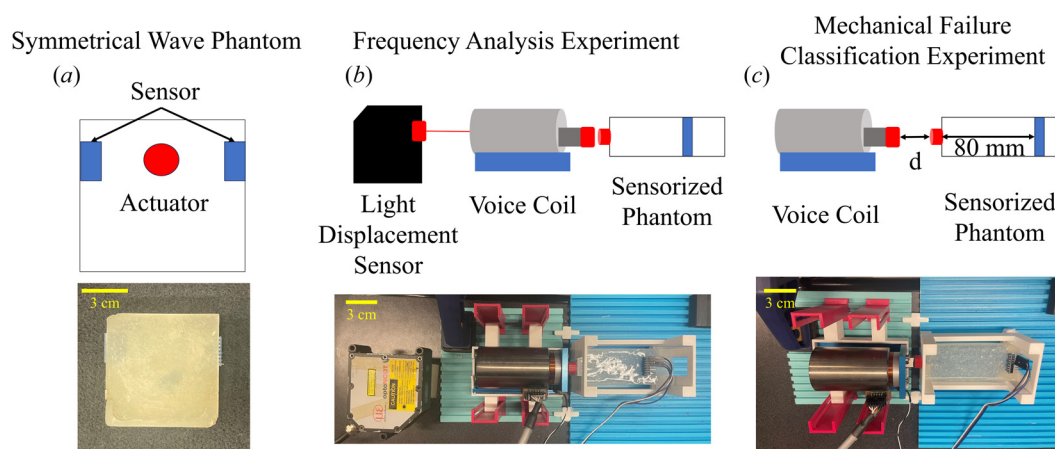n, velocity, and acceleration of the motor. The connections of the experimental setup are displayed in Fig. 3. There are numerous different types of MRE actuators and actuator positioning systems [26–28]. While actuators vary on designs and materials, all MRE actuators typically vibrate at a frequency of 40–150 Hz with the typical clinical standard being 60 Hz [13,29]. Along with this, MRE actuators can be tuned in power or intensity based on body mass index (BMI) to achieve better elastograms [16]. While the current testbed actuator can achieve a max frequency of 20 Hz, the programable parameters provided by the Galil Design Kit allow for tunability in the intensity of the actuation similar to that of typical MRE actuators.

2.2.2 Light Displacement Sensor. An opto-NCDT 2200 light displacement sensor (Micro-Epsilon, Raleigh, NC) was used to experimentally verify the actuation frequency. The sensor is interfaced with an Arduino UNO and is converted into digital readings via a 10-bit analog-to-digital converter (ADC). To measure the frequency, the time was recorded within the Arduino software and the sampling rate was obtained in postprocessing. The obtained sampling rate of the light displacement sensor was 96 Hz.
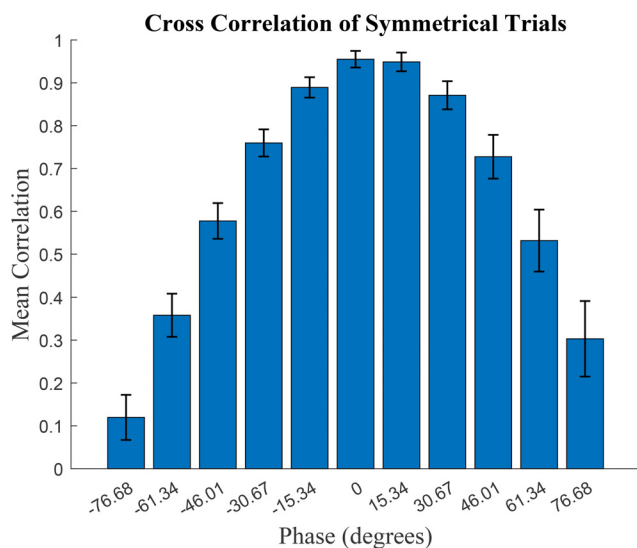
2.3 Phantom Experiments. In order to address proper contact of the MRE actuator, it was critical to verify the capability of the embedded sensors to accurately capture the induced actuation. Two experiments were conducted, as outlined in Fig. 4, to validate the capabilities of the setup and sensor-embedded phantom. The first experiment was to verify that wave propagation throughout the medium was symmetrical as is showcased in Fig. 4(*a*). The second experiment was to verify that the accelerometer readings matched the frequency of the actuation source and this experimental setup is showcased in Fig. 4(*b*). These experiments ultimately inform how shear waves travel throughout the phantom and if there are changes between the actuation signal and the signal received by the accelerometer. The third experiment, Fig. 4(*c*) is to replicate various levels of contact between an actuator and the ROI. Further explanation of the experiment is within Sec. 2.4.1.

2.3.1 Data Processing Procedure. A standardized procedure for filtering the data was conducted for each trial recorded within the experiments. Each trial consists of 1000 data points and the first 100 data points were removed to eliminate transient effects of the actuation source. Afterwards, the data was processed with a 10-point moving average filter and the y-offset of the data was removed.

2.3.2 Symmetrical Sensors Experiment. A phantom was fabricated with two different accelerometers on opposite sides. The

Fig. 4 Experimental setup configurations. (*a*) Symmetrical wave propagation experiment where the accelerometers are equidistant from the actuation source. The actuator was placed at the center between the two accelerometers. (*b*) Frequency analysis experiment where the light displacement sensor was set within the range of actuation and records the frequency of actuation while an embedded phantom was measuring the resulting wave propagation. (*c*) Mechanical failure classification experiment in which the initial distance "*d*" of actuation changes and the resulting wave propagation was measured via an embedded phantom.

Fig. 5 Graph demonstrating the correlation between accelerometers in the symmetrical experiment (*n* = 10)

actuation source was positioned at the center of the phantom equidistant to both accelerometers as shown in Fig. 4(*a*). To obtain the necessary accelerometer positions within the phantom, the accelerometers for this phantom were embedded after the silicone was cured. The phantom was actuated at a frequency of 6 Hz for 10 trials and the data processing procedure was applied. To verify the correlation between the two opposing accelerometers, a cross-correlation test was performed for all 10 trials. Root Mean Square Error (RMSE) was determined between the signals as well. The significance between the two signals was further assessed using a paired sample t-test under the assumption of a normal distribution. Results from the symmetrical experiment are shown in Fig. 5. All 10 trials were found to have the highest correlation at a phase lag of zero. The highest average correlation coefficient was 0.9551 with a standard deviation of 0.0194. In Fig. 5, the cross-correlation and standard deviation are displayed where a phase of 0 was shown to have the smallest standard deviation. A baseline of 0.95 for the correlation coefficient highlights a very strong positive correlation between the two accelerometer signals. The average RMSE of all the trials was 0.0146 with a standard deviation of 0.0015. Since the RMSE was less than 0.02, there was a limited deviation between signals during each trial, which was further exemplified through the paired sample *t*-test ($p = 0.3919$). As the *p*-value was greater than 0.05, we are unable to conclude the signals are different, demonstrating that the shear wave propagation throughout the phantom is relatively uniform.

2.3.3 Frequency Analysis Experiment. In addition to the measurement of symmetrical shear wave vibration, the waveforms were analyzed in the frequency domain to verify the recorded signal waveforms accurately reflect the actuation source frequency. To measure the actuation source frequency, a light displacement sensor was placed behind the voice coil as it actuated against a phantom with an embedded accelerometer, as represented in Fig. 4(*b*). The actuator was tuned to 5, 7, and 9 Hz, and 10 trials were conducted and processed for each of the respective frequencies. A power spectrum was applied to the collected trials of both the light displacement data and the accelerometer data, and the greatest peak was located and recorded within the power spectrum. The light displacement and accelerometer peak frequencies were compared between the trials. All 10 trials from each selected frequency displayed a perfect correlation of 1, indicating no difference between the induced frequency and the frequency measured by the phantom. The agreement of the frequencies between the recorded signal and actuation source was pivotal in ensuring the vibration travels

through the phantom and there is no change in frequency as the actuator interfaces with the phantom.

2.4 Support Vector Machine. Quantification of the frequency and waveforms produced by the MRE actuator provides crucial information on the quality of MRE images, specifically when identifying mechanical and contact failure cases. It was necessary to experimentally simulate both poor and suitable contact of the MRE actuator against the phantom in order to assess different features related to contact. An experiment was designed and conducted using the embedded phantom to simulate varying amounts of contact. Afterward, an SVM algorithm trained and tested by the MATLAB/Simulink (MathWorks, Natick, MA) classification learner was developed to automate the classification of recorded acceleration data from the phantom.

2.4.1 Mechanical Failure Classification Experiments. A custom-embedded phantom was developed with the accelerometer placed 80 mm from the actuation source. The distance *d* as shown in Fig. 4(*c*) was varied from 0 to 840 μm by multiples of 60 (0, 60, 120…) where 0 represents the distance closest to the phantom and 840 the farthest. 10 trials were recorded for each of the distances and the data processing procedure was applied.

2.4.2 Feature Extraction. To conduct the classification with the SVM, 150 trials recorded from the mechanical failure classification were used. Each trial consisted of a variable waveform which can be deconstructed into different features. Features of signals were extracted in both the time domain and frequency domain [30]. A fast Fourier transform was applied to the time domain data resulting in a power spectrum in which frequency features were extracted. The features are outlined in Appendix.

2.4.3 Model Selection and Data Segmentation. For the dataset of 150 trials, data was labeled in which the closest distances (0–180 μm) were "suitable contact" while the rest of the distances (240–840 μm) were labeled as poor contact measurements. A fivefold stratified cross-validation consisting of 128 trials was performed with 22 trials separated for the test dataset. The classification learner was implemented to train various SVM models (Linear, Quadratic, Cubic, Fine Gaussian, Medium Gaussian, and Coarse Gaussian) simultaneously. For each model, the best iteration of the cross-validation was automatically chosen based on classification accuracy. After all models were compared, the best-performing model was selected.

3 Results

3.1 Support Vector Machine Feature Selection. A correlation heatmap as shown in Fig. 6 was created with all the different features extracted from the different domains. The goal of the feature selection was to select a single generalizable feature that was correlated with the distance and then select two other features that were highly correlated with the originally selected feature but had limited correlation with each other. The purpose of the limited correlation consideration was to remove redundancy within the dataset. The first selected feature was the mean absolute value (MAV), as it represented the general power of the dataset and had a relatively strong correlation with the distance (0.673). With the chosen feature of MAV, the secondary features selected were prominence and maximum peak as they were highly correlated with MAV (0.971 and 0.803, respectively), but had a lower correlation with each other when compared to other combinations (0.748). The range and standard deviation of the selected features are showcased in Table 1.

3.2 Support Vector Machine Models and Performance. A breakdown of accuracy and testing performance is shown in Fig. 7 and Table 2. The best model, Fine Gaussian, is plotted with the validation and test dataset in Fig. 8.
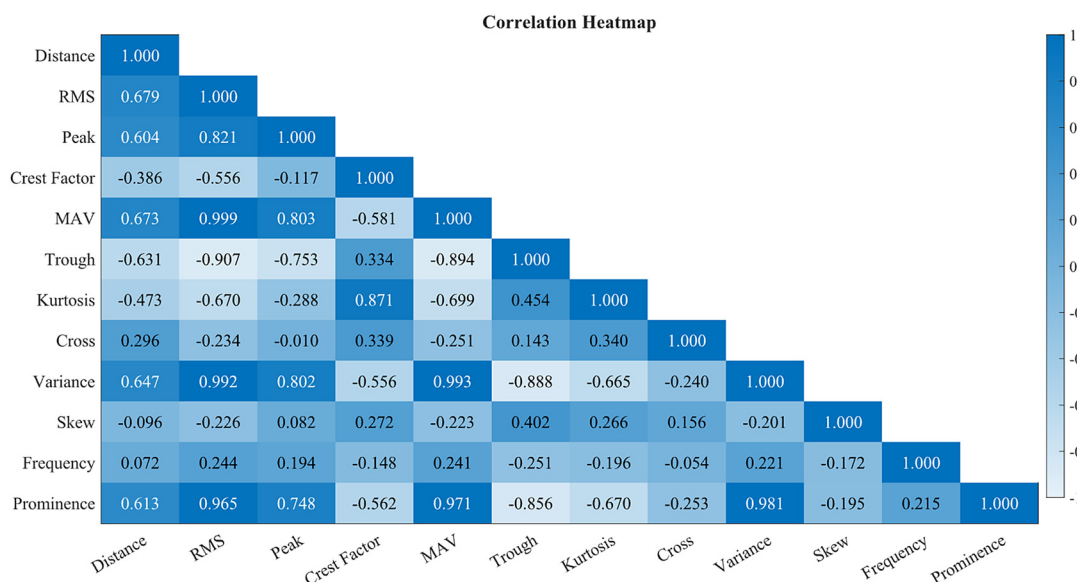
Correlation Heatmap

Fig. 6 Correlation matrix of features from the time and frequency domains

Table 1 Feature selection metrics

Feature	Range	Standard deviation
Peak Acceleration	3.69 cm/s^2	0.65 cm/s^2
Prominence	3.5071×10^{-04}	7.7927×10^{-05}

4 Discussion

Within the presented work, a series of phantoms with embedded accelerometers were developed to measure induced shear waves to help aid MRE actuator testing outside of the clinical setting. By integrating low-profile accelerometers during the phantom curing process, uniform wave propagation throughout the phantom was achieved while also recording the wave propagation. While the system currently cannot be used to fully replicate MRE wave image acquisition, the developed sensor-embedded phantom provides the necessary information needed to assess MRE actuator contact as the system produces acceleration and frequency information, as showcased by both the symmetrical and frequency validation experiments.

When expanding the usage of the developed phantom to detect contact, a stronger signal is expected when the actuator has closer contact with the phantom. The change in signal as the contact distance changes can be seen in Fig. 9, whereas the contact decreases (0–360 μm) there is a negative linear trend ($R = -0.76$) in the recorded signal. At farther distances (360–840 μm), the signal reaches a nonzero asymptote, which is expected as there are residual vibrations within the system. MRE actuators behave in a similar fashion; if the MRE actuator is not above the ROI or the actuator is poorly attached, residual vibrations may only partially illuminate the necessary region, leading to a failure case [31]. While there is a negative linear regression within the area of contact, a lot of the information is lost especially in the poor contact zone shown in Fig. 9. An SVM based on two different features is shown to outperform a linear regression and classifies the data outside the range of the linear regression (360–840 μm). Ultimately, the detection of actuator contact can not be solely based on a single feature and the addition of a second feature within the SVM greatly improves detection accuracy while also expanding the detection range to the entirety of the dataset.

Importantly, all SVM models showcased good accuracy (>80%) in both the validation and testing sets. The selected model (Fine Gaussian) was found to outperform the other models. The breakdown of the validation and test sets, shown in Fig. 8, demonstrates
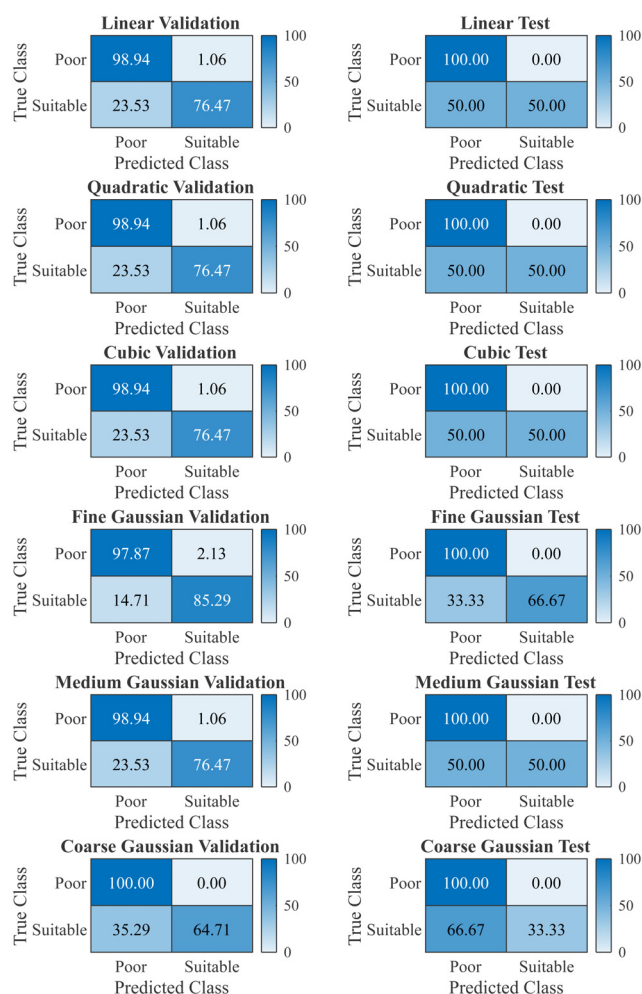

Fig. 7 Confusion matrices of the validation and testing datasets for different SVM models

that all the false positives and negatives are on the border between detection regions. When looking at the Fine Gaussian model and the calculated regions developed from the data, a large majority of the poor contact lies near the bottom left of the graph as showcased in
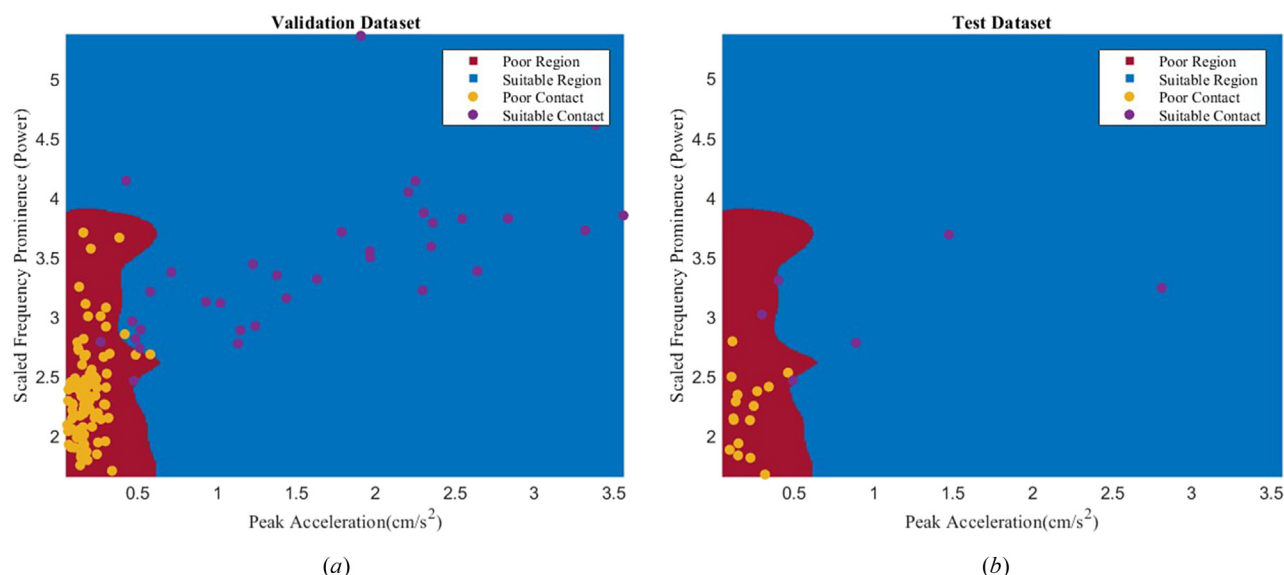
Table 2 Support vector machine model accuracy metrics

Model	Validation (%)	Testing (%)
Linear	92.97	86.36
Quadratic	92.97	86.36
Cubic	92.97	86.36
Fine Gaussian	94.53	90.91
Medium Gaussian	92.97	86.36
Coarse Gaussian	90.62	81.82

added to the SVM during the testing of the models, the addition of noise would only marginally improve the SVM. The nature of the poor contact cases would naturally keep the poor region of the SVM constrained to the bottom left. Noise would impact mainly the data on the border of the poor region and suitable region categories. However, this is a limited part of the dataset, and researchers can account for this by selecting a different model and tuning their model parameters.

For MRE actuator testing, using a sensor-embedded phantom with a machine learning-based classifier can be beneficial in long
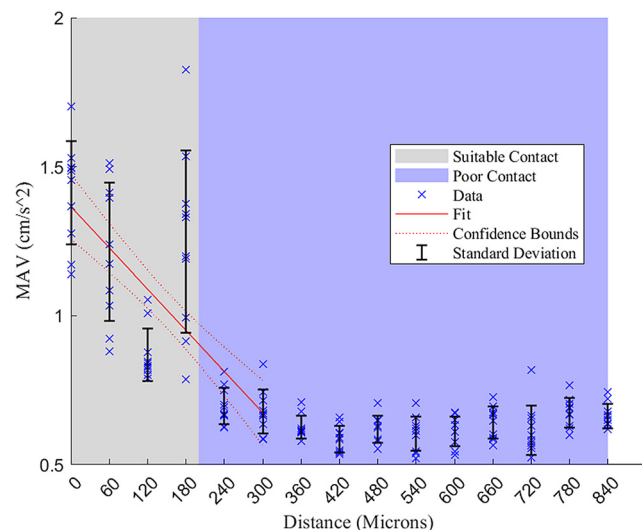

Fig. 8 Selected SVM (Gaussian Model) with validation and test set breakdown: (*a*) the validation dataset was overlaid across the classified regions and (*b*) the test data overlaid across the classified regions.

Fig. 8. As a selected feature for the SVM was peak acceleration, the points near the minimum values are representative of the residual vibrations within the system. When looking at the regions developed by the SVM, there is a boundary in which all the false negatives and positives occur. Researchers may set this boundary as a quantitative benchmark between poor and suitable contact, similar to the boundary created by the SVM. Furthermore, while noise was not

term validation testing. Researchers can retrain an SVM based on their selected MRE actuators, phantom designs, and actuator configurations to best fit their needs. By experimentally collecting data produced by the selected MRE actuator and automating the classification of said data, researchers can quantify a major component of proper illumination without the need for an MRI scanner. Implementation of this system prior to clinical testing will enable extensive testing and iteration on MRE actuators and systems leading to reduced mechanical failures when conducting real MRE procedures.

5 Conclusions

This paper addresses the need for robust MRE actuator testing methodologies outside of the clinical space. A sensor-embedded phantom with an SVM classifier was developed to detect proper contact between the actuator and the phantom. The developed phantom showcased uniform waveform propagation based on the correlation ($R = 0.9551$) while matching the frequency of the programed voice coil. The results of the SVM feature extraction demonstrate contact can be automatically assessed from the data collected from the sensor-embedded phantom. SVM validation and testing accuracy were found to have an almost perfect detection (94.53% and 90.91%) which greatly outperforms potential linear regression models. Future work will consist of increasing the frequency of actuation to verify the capabilities of the system for different MRE procedures, along with utilizing various types of MRE actuators for further validation of the system. The developed system of a sensor-embedded tissue phantom paired with an SVM classifier will provide an automated method to test MRE actuators, ultimately aiding the overall development of MRE.

Fig. 9 Scatter plot of the accelerometer signal collected at different actuator position distances from the phantom. *n* = 10 per distance interval.

Acknowledgment

Funding Data

Data Availability Statement

The datasets generated and supporting the findings of this article are obtainable from the corresponding author upon reasonable request.

Appendix: Frequency Features Extracted for Support Vector Machine

(1) Distance—Actuator starting point from the phantom.

(2) Root mean square (RMS)—The effective power of the signal. n represents the number of measurements, and x_i represents the signal

$$\text{RMS} = \sqrt{\frac{1}{n}\sum_{i=1}^{n}x_i^2} \tag{A1}$$

(3) Peak—The highest point within the dataset. x represents the entire dataset

$$\text{Peak} = \max(x) \tag{A2}$$

(4) Crest factor—The ratio between the peak and the RMS. A representation of the strength of peaks with the dataset

$$\text{CrestFactor} = \frac{\text{Peak}}{\text{RMS}} \tag{A3}$$

(5) Mean absolute value (MAV)—The average magnitude of the dataset. x represents the entire dataset

$$\text{MAV} = \text{mean}(abs(x)) \tag{A4}$$

(6) Trough—The lowest point within the dataset. x represents the entire dataset

$$\text{Trough} = \min(x) \tag{A5}$$

(7) Prominence—The relative strength of the most common frequency compared to other frequencies. f represents the power spectrum dataset

$$\text{Prominence} = \max(f) - \min(f) \tag{A6}$$

(8) Kurtosis—The probability distribution of the dataset. μ^4 represents the fourth central moment and σ_4 is the standard deviation

$$\text{Kurtosis} = \frac{\mu_4}{\sigma^4} \tag{A7}$$

(9) Zero crossing (cross)—The total number of points when the signal changes sign

(10) Variance—The distribution of the signal from the mean value. x_i represents the value of one observation, mean value of observations, and n is the total observations

$$\text{Variance} = \frac{\sum_{i=1}^{n}(x_i - \bar{x})^2}{n - 1} \tag{A8}$$

(11) Skew—The asymmetry of the signal distribution of the acquisition. n represents the total variables, X_i is a variable, $\bar{X}$ is the average of the signal distribution, and σ is the standard deviation

$$\text{Skew} = \frac{\sum_{i=1}^{n}(X_i - \bar{X})^3}{(n - 1) * \sigma^3} \tag{A9}$$

References

[1] Mariappan, Y. K., Glaser, K. J., and Ehman, R. L., 2010, "Magnetic Resonance Elastography: A Review," Clin. Anat., **23**(5), pp. 497–511.

[2] Litwiller, D. V., Mariappan, Y. K., and Ehman, R. L., 2012, "Magnetic Resonance Elastography," Curr. Med. Imaging Rev., **8**(1), pp. 46–55.

[3] Pagé, G., Garteiser, P., and Van Beers, B. E., 2022, "Magnetic Resonance Elastography of Malignant Tumors," Front. Phys., **10**, p. 910036.

[4] Low, G., Kruse, S. A., and Lomas, D. J., 2016, "General Review of Magnetic Resonance Elastography," World J. Radiol., **8**(1), pp. 59–72.

[5] Hiscox, L. V., Johnson, C. L., Barnhill, E., McGarry, M. D., Huston, J., van Beek, E. J., Starr, J. M., and Roberts, N., 2016, "Magnetic Resonance Elastography (MRE) of the Human Brain: Technique, Findings and Clinical Applications," Phys. Med. Biol., **61**(24), pp. R401–R437.

[6] Venkatesh, S. K., Yin, M., and Ehman, R. L., 2013, "Magnetic Resonance Elastography of Liver: Technique, Analysis, and Clinical Applications," J. Magn. Reson. Imaging, **37**(3), pp. 544–555.

[7] Meinhold, W., Ozkaya, E., Ueda, J., and Kurt, M., 2019, "Tuneable Resonance Actuators for Magnetic Resonance Elastography," ASME Paper No. DMD2019-3313.

[8] Morillo-Hernandez, C., Catania, R., Grosse, P. J., Bollino, G., Borhani, A. A., and Furlan, A., 2022, "Magnetic Resonance Elastography of the Liver: A Single-Institution Review of Cases Performed in a 5-Year Interval," J. Comput. Assist. Tomogr., **46**(1), pp. 1–5.

[9] Nieves-Vazquez, H. A., Ozkaya, E., Meinhold, W., Geahchan, A., Bane, O., Ueda, J., and Taouli, B., 2024, "Deep Learning-Enabled Automated Quality Control for Liver MR Elastography: Initial Results," J. Magn. Reson. Imaging., epub.

[10] Anders, M., Meyer, T., Warmuth, C., Pfeuffer, J., Tzschaetzsch, H., Herthum, H., Shahryari, M., Degenhardt, K., Wieben, O., Schmitter, S., et al., 2024, "Rapid MR Elastography of the Liver for Subsecond Stiffness Sampling," Magn. Reson. Med., **91**(1), pp. 312–324.

[11] Kemper, J., Sinkus, R., Lorenzen, J., Nolte-Ernsting, C., Stork, A., and Adam, G., 2004, "MR Elastography of the Prostate: Initial In-Vivo Application," RöFo, **176**(8), pp. 1094–1099.

[12] Hoodeshenas, S., Yin, M., and Venkatesh, S. K., 2018, "Magnetic Resonance Elastography of Liver: Current Update," Top. Magn. Reson. Imaging, **27**(5), pp. 319–333.

[13] QIBA MR Biomarker Committee, 2023, "MR Elastography of the Liver, Clinically Feasible Profile," Quantitative Imaging Biomarkers Alliance, Profile Stage: Clinically Feasible, accessed Nov. 7, 2023, http://qibawiki.rsna.org/index.php/Profiles

[14] Navin, P. J., Venkatesh, S. K., and Ehman, R. L., 2021, "Chapter 90 - MR Elastography," B. D. Ross and S. S. Gambhir, eds., Molecular Imaging, Second Edition, Academic Press, Cambridge, MA, pp. 1759–1774.

[15] Zerunian, M., Masci, B., Caruso, D., Pucciarelli, F., Polici, M., Nardacci, S., De Santis, D., Iannicelli, E., and Laghi, A., 2024, "Liver Magnetic Resonance Elastography: Focus on Methodology, Technique, and Feasibility," Diagnostics, **14**(4), p. 379.

[16] Guglielmo, F. F., Venkatesh, S. K., and Mitchell, D. G., 2019, "Liver MR Elastography Technique and Image Interpretation: Pearls and Pitfalls," Radio-Graphics, **39**(7), pp. 1983–2002.

[17] Steinkohl, E., Bertoli, D., Hansen, T. M., Olesen, S. S., Drewes, A. M., and Frøkjær, J. B., 2021, "Practical and Clinical Applications of Pancreatic Magnetic Resonance Elastography: A Systematic Review," Abdom. Radiol., **46**(10), pp. 4744–4764.

[18] Idilman, I. S., Li, J., Yin, M., and Venkatesh, S. K., 2020, "MR Elastography of Liver: Current Status and Future Perspectives," Abdom. Radiol., **45**(11), pp. 3444–3462.

[19] Triolo, E. R., Khegai, O., Ozkaya, E., Rossi, N., Alipour, A., Fleysher, L., Balchandani, P., and Kurt, M., 2022, "Design, Construction, and Implementation of a Magnetic Resonance Elastography Actuator for Research Purposes," Curr. Protoc., **2**(3), p. e379.

[20] Chakouch, M. K., Charleux, F., and Bensamoun, S. F., 2015, "Development of a Phantom Mimicking the Functional and Structural Behaviors of the Thighmuscles Characterized With Magnetic Resonance Elastography Technique," 2015 37th Annual International Conference of the IEEE Engineering in Medicine and Biology Society (EMBC), Milan, Italy, Aug. 25–29, pp. 6736–6739.

[21] Ozkaya, E., Triolo, E., Rezayaraghi, F., Abderezaei, J., Meinhold, W., Hong, K., Alipour, A., Kennedy, P., Fleysher, L., Ueda, J., Balchandani, P., Eriten, M., Johnson, C., Yang, Y., and Kurt, M., 2021, "Brain-Mimicking Phantom for Biomechanical Validation of Motion Sensitive MR Imaging Techniques," J. Mech. Behav. Biomed. Mater., 122, p. 104680.

[22] McIlvain, G., Ganji, E., Cooper, C., Killian, M. L., Ogunnaike, B. A., and Johnson, C. L., 2019, "Reliable Preparation of Agarose Phantoms for Use in Quantitative Magnetic Resonance Elastography," J. Mech. Behav. Biomed. Mater., 97, pp. 65–73.

[23] Fagerstrom, J. M., and Kaur, S., 2020, "Simple Phantom Fabrication for MRI-Based HDR Brachytherapy Applicator Commissioning," J. Appl. Clin. Med. Phys., 21(11), pp. 283–287.

[24] Bennani, V., Inger, M., and Aarts, J. M., 2014, "Comparison of Pressure Generated by Cordless Gingival Displacement Materials," J. Prosthet. Dent., 112(2), pp. 163–167.

[25] Akkaya, H. E., Erden, A., Kuru Oz, D., Unal, S., and Erden, I., Department of Radiology Karaman State Hospital, Karaman, Turkey 2018, "Magnetic Resonance Elastography: Basic Principles, Technique, and Clinical Applications in the Liver," Diagn. Interventional Radiol., 24(6), pp. 328–335.

[26] Asbach, P., Klatt, D., Hamhaber, U., Braun, J., Somasundaram, R., Hamm, B., and Sack, I., 2008, "Assessment of Liver Viscoelasticity Using Multifrequency MR Elastography," Magn. Reson. Med., 60(2), pp. 373–379.

[27] Feng, Y., Zhu, M., Qiu, S., Shen, P., Ma, S., Zhao, X., Hu, C.-h., and Guo, L., 2018, "A Multi-Purpose Electromagnetic Actuator for Magnetic Resonance Elastography," Magn. Reson. Imaging, 51, pp. 29–34.

[28] Meinhold, W., Ozkaya, E., Petti, D., Rice, V., Triolo, E., Rezayaraghi, F., Kennedy, P., Fleysher, L., Hu, A.-P., Ueda, J., and Kurt, M., 2022, "Towards Image Guided Magnetic Resonance Elastography Via Active Driver Positioning Robot," IEEE Trans. Biomed. Eng., 69(11), pp. 3345–3355.

[29] Ehman, E. C., Rossman, P. J., Kruse, S. A., Sahakian, A. V., and Glaser, K. J., 2008, "Vibration Safety Limits for Magnetic Resonance Elastography," Phys. Med. Biol., 53(4), pp. 925–935.

[30] Ramón, M. M., Atwood, T., Barbin, S., and Christodoulou, C. G., 2009, "Signal classification With an SVM-FFT Approach for Feature Extraction in Cognitive Radio," 2009 SBMO/IEEE MTT-S International Microwave and Optoelectronics Conference (IMOC), Belem, Brazil, Nov. 3–6, pp. 286–289.

[31] Pepin, K. M., Welle, C. L., Guglielmo, F. F., Dillman, J. R., and Venkatesh, S. K., 2022, "Magnetic Resonance Elastography of the Liver: Everything You Need to Know to Get Started," Abdom. Radiol., 47(1), pp. 94–114.